

Where is the Super-Virial Gas? The Supply from hot inflows

MANAMI ROY,^{1,2} KUNG-YI SU,³ SMITA MATHUR,^{1,2} AND JONATHAN STERN⁴

¹*Center for Cosmology and Astro Particle Physics (CCAPP), The Ohio State University, 191 W. Woodruff Avenue, Columbus, OH 43210, USA*

²*Department of Astronomy, The Ohio State University, 140 W. 18th Ave., Columbus, OH 43210, USA*

³*Black Hole Initiative, Harvard University, 20 Garden St., Cambridge, MA 02138, USA*

⁴*School of Physics & Astronomy, Tel Aviv University, Tel Aviv 69978, Israel*

ABSTRACT

In an effort to understand the presence of super-virial gas detected in the Milky Way, we present our findings from isolated galaxy simulations of Milky Way-like systems using GIZMO with the FIRE-2 (Feedback In Realistic Environments) stellar feedback model. It unveils the presence of a significant super-virial temperature ($T > 6 \times 10^6 \text{K}$) gas component within 20 kpc from the galactic center. This super-virial gas has a mass of $1 - 2 \times 10^7 M_{\odot}$ and is found close to the disk, where typical gas densities are $0.004 - 0.01 \text{cm}^{-3}$. We find that some of the virial gas ($T \sim 10^6 \text{K}$) forms a rotating hot inflow, where gravitational energy is converted to heat mainly via compressive heating. This process causes gas infalling close to the rotation axis to reach super-virial temperatures just before cooling and joining the disk. Stellar feedback heating accounts for less than 1% of the super-virial gas, indicating its minimal influence despite expectations. Even in scenarios with no stellar feedback effects considered, abundant super-virial gas persists, highlighting the dominance of alternative heating mechanisms. We also show that cosmic rays do not have a significant effect on heating the gas to a super-virial temperature. Our study illuminates the intricate dynamics of hot virial and super-virial gas surrounding Milky Way-like galaxies, emphasizing the prominent role of infall-driven and compressive heating processes in shaping thermal evolution.

Keywords: Galaxy: evolution — Galaxy: halo — methods: numerical — (ISM:) cosmic rays — (galaxies:) quasars: absorption lines — X-rays: galaxies

1. INTRODUCTION

Galaxies are the building blocks of our universe and how galaxies form and evolve is an active area of research. A spiral galaxy has two main components, a star-forming disk and a diffuse gaseous halo surrounding the disk. This diffuse gaseous halo, known as Circumgalactic medium (CGM) (Tumlinson et al. 2017; Faucher-Giguère & Oh 2023), plays a crucial part in galaxy evolution. The CGM is the habitat for large-scale gas flows that fundamentally regulate the evolution of the galaxy by providing fresh and recycled gaseous fuel for star formation and regulating the galaxy’s interactions with other galaxies. A comprehensive understanding of the CGM stands to illuminate key unresolved

questions pertaining to the processes driving galaxy formation and evolution.

Unfortunately, the CGM is very hard to detect in emission due to its very low density. However, from absorption lines in the spectra of background quasars, we can infer about the physical properties of the CGM. When light from a background quasar passes through the CGM of a galaxy, it suffers absorption from the metals and ions in the CGM. Absorption studies made by COS spectrograph onboard HST along with XMM-Newton and Chandra has enabled us to detect this multiphase diffuse gas around Milky Way (MW) mass galaxy in UV [e.g. Tumlinson et al. (2011); Werk et al. (2016)] and X-ray [e.g. Gupta et al. (2012); Fang et al. (2015); Das et al. (2021); Mathur (2022)] respectively. In the X-ray band, the MW CGM has been detected in X-ray emission as well [e.g. Snowden et al. (2000); Henley & Shelton (2013); Nakashima et al. (2018).]

Until 2019, These observations led us to a picture where the CGM is multi-phase in nature and has three main components; virial temperature warm-hot gas ($T \sim 10^{6-6.5}$ K), warm gas ($T \sim 10^{5-5.5}$ K) and cool gas ($T < 10^4$ K). However this picture got modified with the recent discovery of the super-virial component ($T \sim 6 \times 10^6 \text{K} - 2 \times 10^7 \text{K}$; Das et al. (2019b)) in the MW CGM using absorption lines from XMM-Newton observation towards the Blazar IES 1553+113. Since then, there have been multiple detections of this hotter super-virial gas in both emission and absorption (Das et al. 2019a; Gupta et al. 2023; Bhattacharyya et al. 2023; Lara-DI et al. 2023; McClain et al. 2024). In emission, Das et al. (2019a) detected the super-virial component towards the same sight-line of Blazar IES 1553+113 using XMM-Newton, and Gupta et al. (2023) found this component along with virial component along four sight-lines from Suzaku and Chandra. Later, Bhattacharyya et al. (2023) also detected this super-virial gas in the MW CGM in emission towards the Blazar Mrk 421 and 5 other sightlines near the Blazar field. Even in a recent study by McClain et al. (2024) detected SiXIV $K\alpha$ and SXVI $K\alpha$, associated with a gas phase with super-virial temperature, in the CGM of the MW, with the use of stacked X-ray spectral observations towards multiple of different extragalactic sightlines.

This super-virial component has not only been detected towards some particular sightlines, but all-sky surveys from Halo-Sat and eROSITA have also found this component abundantly in all over the sky. Bluem et al. (2022) utilized data from the HaloSat all-sky survey to delve into the emissions originating from the MW’s halo and detected the supervirial gas. Ponti et al. (2023), in their study of the MW halo within the eFEDDS field employing eROSITA, also detected this component.

However, the gas at these temperatures defies the predictions of galaxy formation simulations (e.g., Shen et al. (2013)). Its discovery begs the questions like: *where is this gas situated; in the ISM, inner CGM or outer CGM? How this gas is formed; through feedback or some other heating mechanisms like cosmic ray (CR) heating? What is the nature of this gas; is it as diffuse as the volume filling virial temperature gas or is it more or less dense?*

In this paper, we will address above questions in light of an idealized simulation. We investigate a suite of simulations of MW-type hosts where we focus on these super-virial gas components. The paper is structured as follows. In Section 2, we discuss the methodology of our simulation, where we describe the initial conditions of our simulation setup (in Section 2.1) along with

our definition of super-virial CGM gas for our analysis (in Section 2.2). In Section 3, we demonstrate our results from our analysis of the simulations, where we discuss the location (Section 3.1), density (in Section 3.2), amount (Section 3.3), and origin (Section 3.4) of the super-virial gas in the CGM. We also discuss if feedback and cosmic rays heating have any effect on the origin of this gas in Section 3.1 and 3.3. We discuss the limitations of our work and planned future work in Section 4. Finally, we summarize our results and discuss future work in Section 5.

Table 1. Summary of all the runs

Symbol	Resolution	Feedback	Cosmic Ray
m12_lr	low	Yes	No
m12_hr	high	Yes	No
m12_lr_nofb	low	No	No
m12_lr_CR_low	low	Yes	Yes (low)
m12_lr_CR_high	low	Yes	Yes (high)
m12_lr_CF (cooling flow)	low	Yes	No

2. METHODOLOGY

Our simulations utilize GIZMO¹ (Hopkins 2015), in its meshless finite mass (MFM) mode, which is a Lagrangian mesh-free Godunov method, capturing the advantages of grid-based and smoothed-particle hydrodynamics (SPH) methods. Numerical implementation details and extensive tests are presented in a series of methods papers for, e.g., hydrodynamics and self-gravity (Hopkins 2015), magnetohydrodynamics (MHD; Hopkins & Raives 2016; Hopkins 2016), anisotropic conduction and viscosity (Hopkins 2017; Su et al. 2017), and cosmic rays (Chan et al. 2019a).

In all simulations except for the runs with no feedback, we incorporate the FIRE-2 model, an implementation of the Feedback In Realistic Environments (FIRE) approach. This encompasses treatments of the interstellar medium (ISM), star formation, and stellar feedback, the details of which are given in Hopkins et al. (2018a,b) along with extensive numerical tests. Our simulations cover a broad temperature range from 10 to 10^{10} K, accounting for various cooling mechanisms including photoelectric and photoionization heating, collisional, Compton, fine structure, recombination, atomic, and molecular cooling.

¹ A public version of this code is available at <http://www.tapir.caltech.edu/~phopkins/Site/GIZMO.html>

Star formation is facilitated through a sink particle approach, allowed only in molecular gas regions with densities surpassing 100cm^{-3} , where self-shielding and local self-gravitation dominate. Upon formation, star particles are treated as cohesive stellar populations, inheriting the metallicity of their parent gas particles. Feedback mechanisms, including supernovae and mass-loss rates, are derived from IMF-averaged values calculated from STARBURST99 (Leitherer et al. 1999) with a Kroupa initial mass function (IMF) (Kroupa 2002).

The stellar feedback model encompasses diverse processes: (1) Radiative feedback, involving photo-ionization, photo-electric heating, and single and multiple-scattering radiation pressure tracked in five bands (ionizing, FUV, NUV, optical-NIR, IR), (2) Continuous stellar mass loss and injection of mass, metals, energy, and momentum through OB and AGB winds, and (3) Type II and Ia supernovae (including both prompt and delayed populations), injecting appropriate mass, metals, momentum, and energy into the surrounding gas based on tabulated rates. All the simulations integrate magnetohydrodynamics (MHD), fully anisotropic conduction, and viscosity, employing the Spitzer-Braginski coefficients to capture the relevant physics.

The model for cosmic ray (CR) treatment includes streaming, which occurs at the local Alfvén speed or sound speed, whichever is larger, incorporating an appropriate streaming loss term that thermalizes energy, as described in Uhlig et al. (2012). Diffusion is modeled with a fixed diffusivity $\sim 3 \times 10^{28} \text{cm}^2\text{s}^{-1}$, alongside adiabatic energy exchange between gas and CR pressure, and includes hadronic and Coulomb losses (following Guo & Oh (2008)). We consider a single energy bin for GeV CRs, which dominate the pressure, and treat them in the ultra-relativistic limit. Both streaming and diffusion are fully anisotropic along magnetic field lines. CRs are injected by supernovae (SNe), with 10% of each SNe energy being transferred into CRs, consistent with studies like Pfrommer et al. (2017a,b). For details on cosmic ray physics is demonstrated in Su et al. (2019a); Chan et al. (2019b).

2.1. Initial conditions

The initial setup closely follows the detailed specifications outlined in Su et al. (2019b); Roy et al. (2024). To further stabilize the host CGM, the simulation region is expanded to 3 times the virial radius, and the simulations are run adiabatically (no cooling or star formation) for 4.5 Gyr for relaxing any initial transients before the satellites are placed into the CGM. The simulation properties are summarized in table 1 of Roy et al. (2024). In

this paper, we only focus on the **m12** halo which is corresponding to the MW-like halo of mass $\sim 1.8 \times 10^{12} M_{\odot}$.

We consider only the runs with 20 satellites of $2 \times 10^9 M_{\odot}$ DM halo mass (**20xm09**). We vary different physical properties to test the impact of the stellar feedback and cosmic rays. We summarize all of our runs in Table 1.

We initialize the dark matter (DM) halo, bulge, black hole, and gas+stellar disk of m12 by following Springel & White (1999); Springel (2000). The initial metallicity goes down from solar ($Z = 0.02$) to $Z = 0.001$ with radius as $Z = 0.02 (0.05 + 0.95/(1 + (r/20 \text{ kpc})^{1.5}))$. Magnetic fields are initialized azimuthal with $|\mathbf{B}| = 0.03 \mu\text{G}/(1 + (r/20 \text{ kpc})^{0.375})$. For our cooling flow run, we have the same initial condition but with a cooling flow solution with cooling flow of roughly $5 M_{\odot} \text{yr}^{-1}$, a sonic radius of 1 kpc and a circularized radius of 10 kpc (following Stern et al. 2024). We initialize CRs in the high CR runs such that the CR energy density is in equipartition with thermal energy density. In this case, we decrease the temperature by half, keeping the density same, and put the rest of the energy in CR. So the pressure gradient is maintained. In low CR runs, CRs are initialized such that the CR energy density is in equipartition with magnetic energy density, which is ~ 5 order of magnitude lower than the thermal energy density.

We initialize the satellites similarly as the host described above, though without a CGM gas halo. The properties are also summarized in table 1 of Roy et al. (2024). More details of initial set up is described in Methodology section of Roy et al. (2024).

2.1.1. Gas temperature of the initial condition

All the runs have similar initial setup except for the high CR run. We check that our initial setups for different runs do not contain any super-virial gas. We confirm that the initial temperature is not more than $4 \times 10^6 \text{K}$ in all the runs. In the high CR run, the initial temperature profile is even lower for maintaining hydro-static pressure balance, not crossing $2 \times 10^6 \text{K}$. The variation in the initial condition will be useful to test whether the super-virial gas can be found even with a cooler halo, and test whether the results are sensitive to the initial set-up. We also confirm that the initial density ranges similarly in all the cases, with virial gas having density $10^{-(3-4)} \text{cm}^{-3}$.

2.2. Defining Super-virial Gas

Observationally, the gas with temperature $6 \times 10^6 - 2 \times 10^7 \text{K}$ has been identified as super-virial phase. For this analysis, we use temperature cut of $6 \times 10^6 \text{K}$ for super-

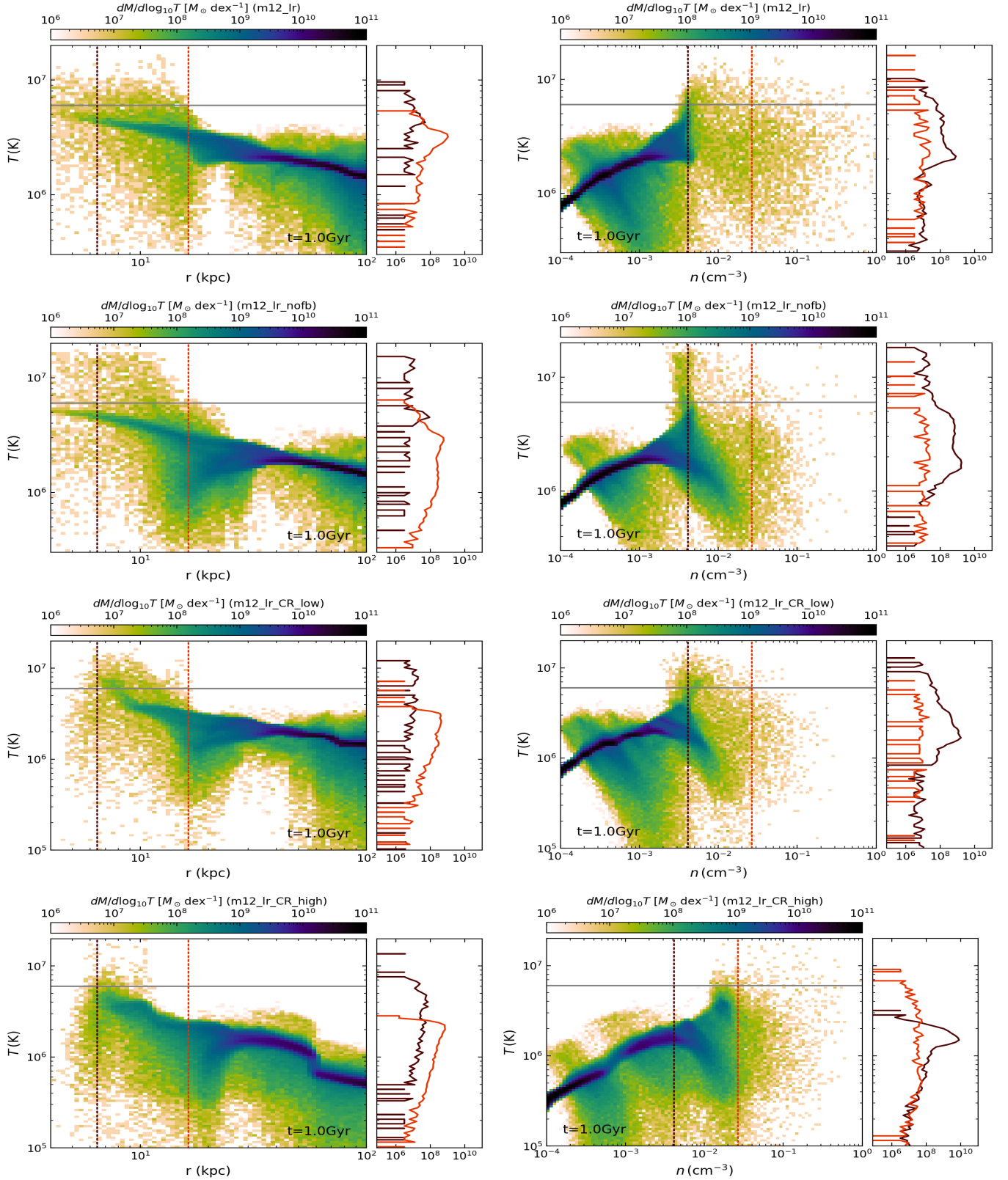


Figure 1. 2D probability distribution function (PDF) of gas temperature, weighted by mass, with respect to position (left panels) and density (right panels) for the different simulations at snapshot $t = 1$ Gyr. The rows represent different scenarios: no cosmic rays (top row), no cosmic rays and no feedback (second row), low cosmic rays (third row), and high cosmic rays (bottom row). The right bar of each 2D histogram shows 1D histograms of temperature at specific positions and densities, indicated by the vertical colored lines in the corresponding 2D histograms. The horizontal line marks the temperature cutoff of 6×10^6 K, indicating the threshold for super-virial gas. The temperature profiles reveal the presence of super-virial gas in all simulation runs, with this gas located within 20 kpc of the galaxy center. The density of the super-virial gas is much higher than the average density of the virial gas.

virial gas. Therefore, we consider gas with temperature above this threshold to be called as ‘super-virial’.

3. RESULTS

3.1. Where is the super-virial gas?

This section delves into the investigation of the distribution of supervirial gas within the simulation box. We present the 2-d PDFs of temperature of the gas weighted by its mass with the variation of its position and density, in the left and right panels of Figure 1 respectively. The 2d-PDFs denote the four different runs at 1 Gyr snapshot of the simulation for no CR (1st row), no CR and no Feedback (2nd row), low CR (3rd row), and high CR (bottom panel) cases.

In all the 2-d distribution plots, we did a radial cut of 6 times of the gas scale radius region around the satellites to exclude the ISM of the satellites, as we choose this radius of the satellite to be the radius beyond which the gravitational pull from the satellites is negligible. Note, however, that we do not exclude satellite particles which get stripped from the satellites. The horizontal line in Figure 1 denotes the super-virial temperature cut of 6×10^6 K; gas with temperature above this threshold is called ‘super-virial’.

In the right bar of each 2-d histogram plot in Figure 1, we show the 1-d histograms of mass-weighted temperature at two different positions (left panels) and density (right panels) denoted by the similarly colored vertical lines in the 2-d histograms. For example, in the left panel of Figure 1, there is a red vertical line at 20 kpc and the corresponding histogram in the right bar, showing the temperature distribution at 20 kpc. We see that the distribution not extends above 6×10^6 K. On the other hand, the temperature distribution shown by the black histogram (corresponding to 6.5 kpc) extends far beyond 6×10^6 K. Therefore, we conclude that the majority of the super-virial gas is concentrated within a 20 kpc radius across all of the simulation runs.

We also checked if we can see this gas at an earlier snapshot at $t=0.5$ Gyr and we found it for all of cases except for the high CR one, where the super-virial gas is not there at 0.5 Gyr, but appears at 1 Gyr. This is mainly due to the fact that the high CR runs have cooler initial halo, therefore taking longer time to get heated.

In summary, we investigate the distribution of super-virial gas within the simulation box, initially examining its temperature and density distributions. Excluding regions around satellites, the analysis reveals that the majority of super-virial gas, exceeding 6×10^6 K, is concentrated within a 20 kpc radius across all runs. Notably, the high CR runs exhibit delayed appearance of super-virial gas at 1 Gyr due to cooler initial halo

conditions, highlighting sensitivity to initial setup and heating dynamics.

3.2. How dense is the super-virial gas?

In this section, we scrutinize the density distribution of the super-virial gas. In the right panel of Figure 1, we present 2D histograms illustrating the relationship between temperature and density, weighted by mass. It shows the temperature evolution of 2-d probability distribution function (PDF) of gas mass as a function of the temperature and density of the gas at $t=1$ Gyr for no CR (1st row), no CR and no Feedback (2nd row), low CR (3rd row), and high CR (bottom panel) cases. In these plots, we excluded the region around the satellites like before. Notably, in all the cases, the density of the super-virial gas is approximately $3 \times 10^{-(2-1)} \text{ cm}^{-3}$ as the gas is closer to the disk, as shown in left panel of Figure 1.

3.3. How much super-virial gas is there in the galaxy?

Next, we quantify the mass of super-virial gas present in the galaxy. Given that the bulk of the super-virial gas resides within a 20 kpc radius, we depict the temporal evolution of super-virial gas masses within 20 kpc and 10 kpc using solid and dashed lines, respectively, in Figure 2. Here, we do not exclude the region around the satellites, as we would like to check if satellites also contributes to this gas phase. However, as the satellites are in circular orbits between 100kpc and 150kpc, the regions around them are automatically cut out while we calculate super-virial gas mass inside 20 kpc and 10 kpc. Key insights from this analysis include:

- **Mass:** The mass of super-virial gas fluctuates within the range of $1 - 2 \times 10^7 M_\odot$ throughout the entire 1.5 Gyr simulation period within 10 kpc, with 2 times larger mass within 20kpc. CGM gas mass being $2 \times 10^{11} M_\odot$, the supervirial gas is only 0.1-1% of the total CGM gas, hence sub-dominant in the baryonic budget and does not contribute to the missing baryon problem.
- **Effect of Feedback:** The presence of the super-virial gas could have been a direct result of heating by stellar feedback. Therefore, if we don’t include feedback in our simulations, we might expect no (or significantly smaller amount of) super-virial gas. Surprisingly, however, the simulations with no feedback display a higher and similar amount of mass of super-virial gas among all the runs. This shows that in our simulations, the stellar feedback is not predominantly responsible for generating the super-virial gas.

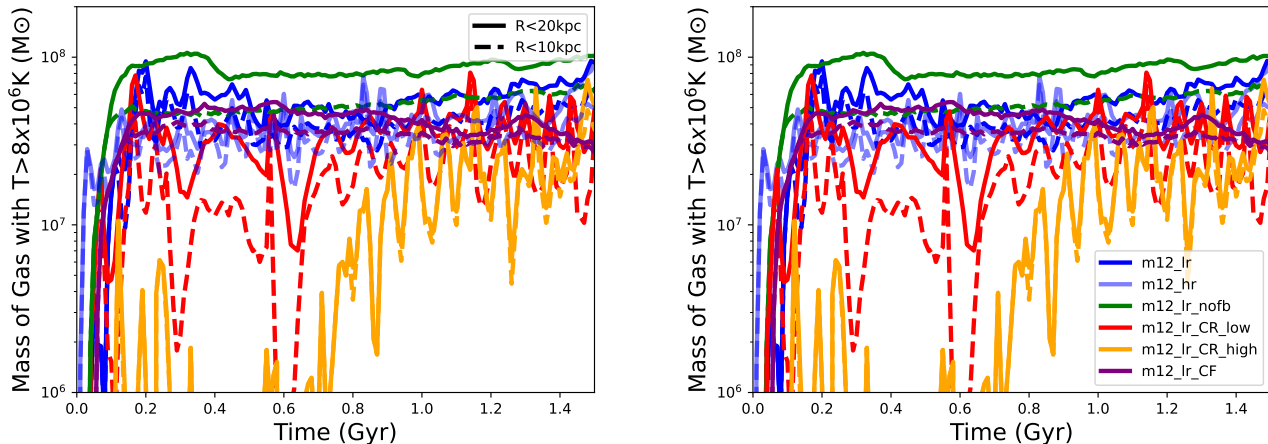


Figure 2. Time evolution of the super-virial gas mass in various simulation runs, comparing two temperature cutoffs (left panel: $T > 8 \times 10^6 \text{K}$, right panel: $T > 6 \times 10^6 \text{K}$). Solid and dashed lines represent the gas mass within 20 kpc and 10 kpc, respectively. The figure demonstrates the persistent presence of supervirial gas across different runs, including those without stellar feedback. Notably, substantial amounts of supervirial gas are retained even in simulations with cosmic rays and varying initial conditions, such as the cooling flow and high cosmic ray runs.

- **Effect of Cosmic Rays:** CR heating by streaming heating or Coulomb heating can be one of the heating source of the super-virial gas. It can also drive outflow that can heat the gas. We investigate this with two runs with CRs, one with low CR and one with high CR. Minimal disparities exist between CR and no CR runs. The runs incorporating CRs exhibit slightly more pronounced mass fluctuations compared to runs without CRs, with the high CR run showing an even larger fluctuations. Hence, in our simulations, the CR is not predominantly responsible for heating the gas to super-virial phase.
- **Effect of Resolution:** We have conducted higher-resolution simulations (10 times higher resolution compared to our low resolution run), represented by dashed lines in Figure 2. Our anticipation was that these high-resolution (hr) runs would capture denser, super-virial gas compared to the low-resolution (lr) counterparts. We observe that the super-virial gas mass in the hr runs qualitatively similar to that in the lr runs. This consistency suggests that our findings remain robust across varying levels of resolution.
- **Effect of Other Satellite Runs:** We also check the other satellite runs described in Roy et al. (2024), with m10 and m08 satellites to check whether the satellite distribution has a significant effect on our results (not shown in the figure). We find that there is no significant difference in the

super-virial gas mass budget with the difference in satellite distribution.

In summary, we find that the temporal evolution of super-virial gas mass within 20 and 10 kpc radii reveals fluctuations between $1 - 2 \times 10^7 M_{\odot}$, with a doubling of mass within the broader radius, constituting only 0.1-1% of the total CGM gas mass. Surprisingly, simulations without feedback display higher and more consistent super-virial gas masses, suggesting super-virial gas does not predominantly originate from feedback heating processes. Minimal disparities in super-virial gas mass fluctuations are observed between runs with and without cosmic rays, with higher CR runs showing slightly more pronounced fluctuations.

3.4. Where is the super-virial gas coming from?

Now the question is what is the mechanism by which this gas is heated. As noted above, CR heating and feedback heating do not seem to be responsible for heating to super-virial temperatures in our simulations. Therefore, we track the host gas particles with initial temperature $T_{\text{ini}} \sim 2 \times 10^6 \text{K}$, which reached their maximum temperature at a simulation time of 1 Gyr. We calculate the past temperature, density, and spherical radius of all such gas particles (host and satellite). We find that there are three sets of gas particles that contribute to the super-virial phase, with two sets from the host and one from the satellites. One set has initial temperature similar to the virial gas $2 \times \sim 10^6 \text{K}$ (set-1 hereafter) whereas other set has initial temperature of a cold gas 10^4K (set-2 hereafter). There are another set (set-3 hereafter), which are gas particles, initially coming from

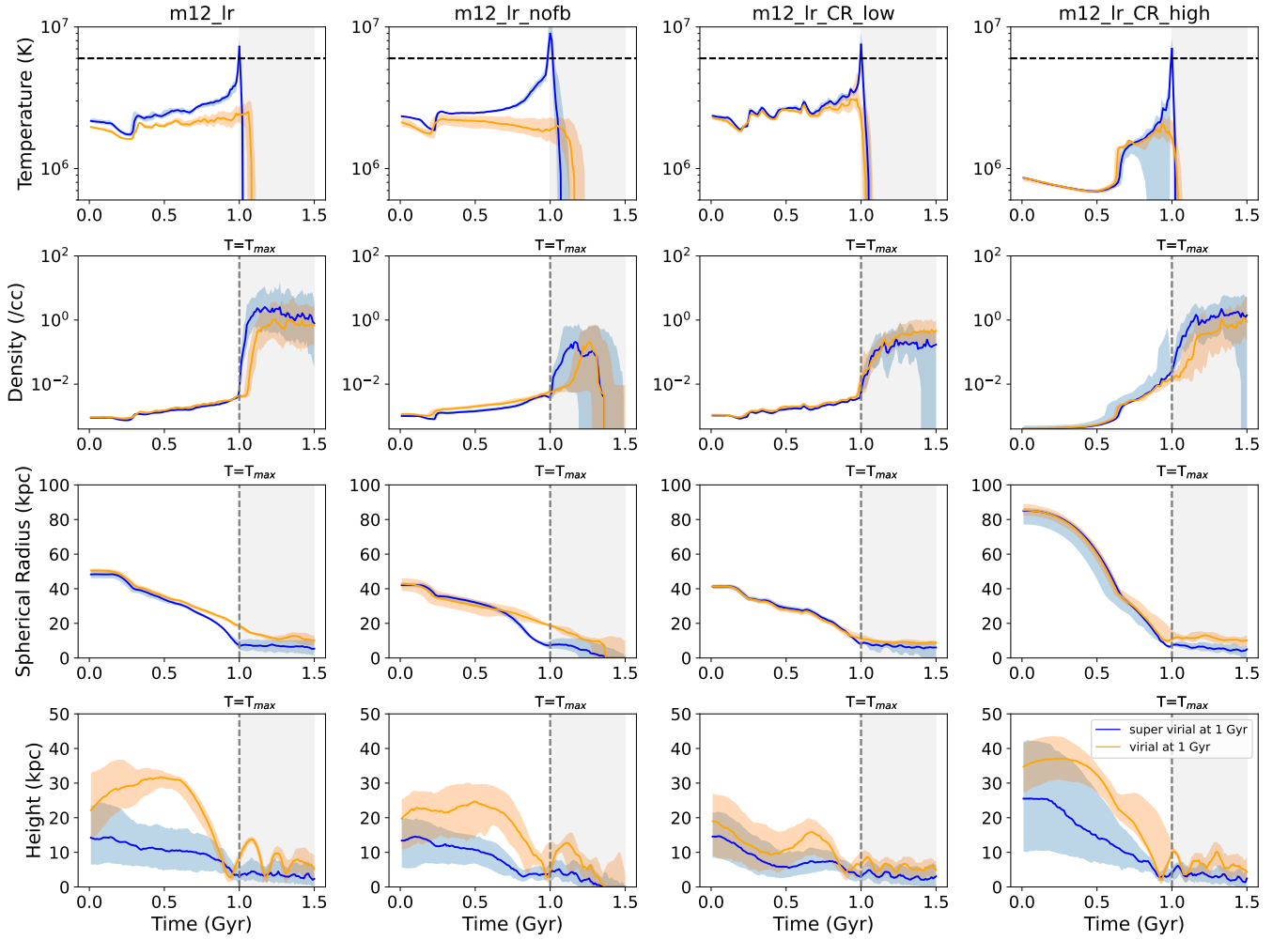
Set-1: Host Gas Particles, $T_{ini} \sim 2 \times 10^6 K$


Figure 3. Time evolution of the temperature (top row), density (2nd row), spherical radius (3rd row), and scale height (bottom row) of the host gas particles with initial temperature $T_{ini} \sim 2 \times 10^6 K$, which reached their maximum temperature at a simulation time of 1 Gyr. Blue and orange indicate gas with super-virial and virial temperatures at 1 Gyr, respectively. The solid lines represent the median values of the gas properties, while the shaded regions indicate the dispersion. The blue curves illustrate how infalling gas initially at virial temperatures is heated to super-virial temperatures through compressive heating just before cooling and joining the ISM disk.

satellites and found to be at super-virial temperature. We plot median and dispersion of properties of all these particles for each cases. We list the properties of set-1, set-2 and set-3 particles below :

3.4.1. Set-1: Host gas particles, $T_{ini} \sim 2 \times 10^6 K$

In Figure 3, blue curves show the time evolution of the temperature (top row), density (2nd row), spherical radius (3rd row), and scale height (bottom row) of host gas particles with initial temperature $T_{ini} \sim 2 \times 10^6 K$, which reached their maximum temperature at a simulation time of 1 Gyr. These gas particles have initial temperature $\sim 2 \times 10^6 K$ in all the case except for high

CR run where the initial temperature was $\sim 1 \times 10^6 K$. This is because for high CR case, the initial halo has a lower thermal pressure, and in turn a lower temperature-halo. The Figure shows that gas heats up slowly over time and reaches over $6 \times 10^6 K$ at $t=1$ Gyr.

In the second row of Figure 3, we plot past density of these super-virial gas particles. All of them start from 10^{-3}cm^{-3} , which is a typical density of the diffuse virial gas. Following their rise to super-virial temperatures at 1 Gyr, they cool down, reducing their density to $1, \text{cm}^{-3}$. Again high CR run starts from the lower density of $5 \times 10^{-4} \text{cm}^{-3}$ than the density of other runs, as we are tracking the gas particles from a larger radius

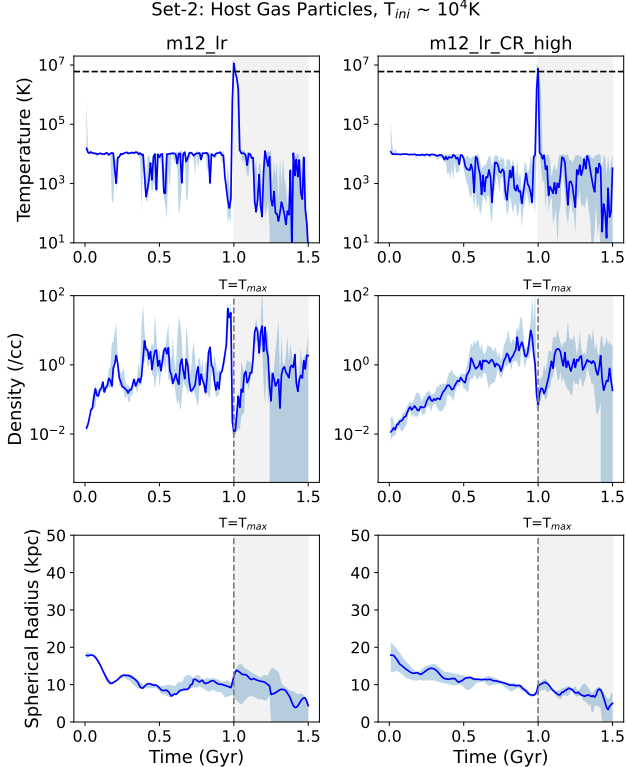


Figure 4. Time evolution of the temperature (top row), density (2nd row), and spherical radius (bottom row) of the host gas particles with initial temperature $T_{\text{ini}} \sim 10^4$ K, which reached their maximum temperature at a simulation time of 1 Gyr. The solid line represents the median values of the gas properties, with the shaded regions indicating the dispersion. The figure illustrates how cold gas of disk is heated to super-virial temperatures due to feedback heating. These gas particles are missing in no feedback runs and have a sub-dominant contribution to the super-virial phase in all other runs.

as we mention in next paragraph. But eventually they reach the same final density as all the other runs. Therefore, there is almost a factor of 2000 and 1000 increase in density in high CR and all the other cases respectively.

In the third panel of Figure 3, we plot the time evolution of the position of these super-virial gas. All of them are falling from outer halo (50-80 kpc) into the central 10 kpc region. For all the other cases the particles fall from 40-50 kpc whereas for high CR run, the gas particles fall from little farther away, 80-90 kpc.

As the gas particles fall inwards, they start heating up as this infall changes the gravitational potential energy, which can be converted to thermal energy and slowly heat up the gas. Until 0.9 Gyr, the temperature only increases to $3 - 4 \times 10^6$ K. At 0.9 Gyr, these gas particles roughly reach 10 kpc which is the radius of Galactic disc. At that point, they get compressed by going from

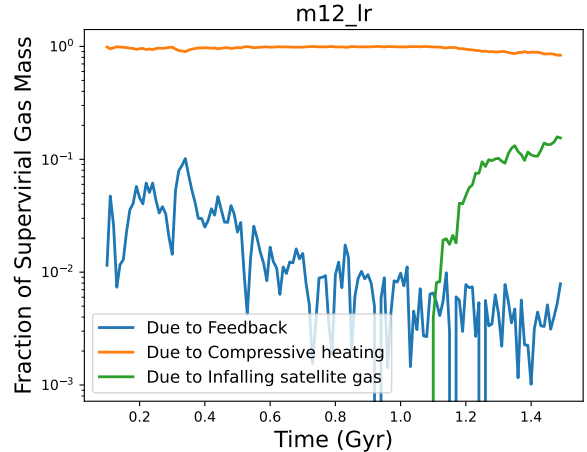


Figure 5. Fraction of super-virial gas mass attributed to stellar feedback (initial temperature $T_{\text{ini}} \sim 10^4$ K) and compressive heating of infalling gas (initial temperature $T_{\text{ini}} \sim 2 \times 10^6$ K) in the case of our fiducial run. The figure shows that feedback contributes approximately 1% to the super-virial gas mass in our simulations, while infalling virial gas is the dominant contributor to the super-virial phase. Infalling satellite gas also starts to contribute 3% at $t=1.2$ Gyr, increasing their contribution to 10% at $t=5$ Gyr.

spherical to disc geometry, as shown by bottom-most row of Figure 3. And due to this compression, the gas is heated to over 6×10^6 K and becomes super-virial gas. Therefore, it is clear that set-1 gas particles are infalling onto the disc and they are heated up by compression, and hence we see enhancement of density and temperature. Once they heat up to the super-virial phase, they cool down immediately because they become rotationally supported and radiate thermal energy away after they join the disc, as shown by the time evolution of the spherical radius r , which does not decline and remains constant after $t = 1$ Gyr. Please note that the smooth evolution of the density and temperature curves suggests the heating is compressive rather than shocks, as shown by tracking of individual particles in Figure 3.

3.4.2. Set-2: Host gas particle, $T_{\text{ini}} \sim 10^4$ K

In the top row of Figure 4, we plot the time evolution of the temperature (top row), density (2nd row), and spherical radius (bottom row) of the host gas particles with initial temperature $T_{\text{ini}} \sim 10^4$ K, which reached their maximum temperature at a simulation time of 1 Gyr. The gas particles in these sets are very few except for high CR case and absent in no feedback case. These gas particles get colder and hotter over time by fluctuating between 10^4 K and 10K until 0.9 Gyr where the gas heats up and reaches over 6×10^6 K at about 1 Gyr. These gas particles are probably heating from stel-

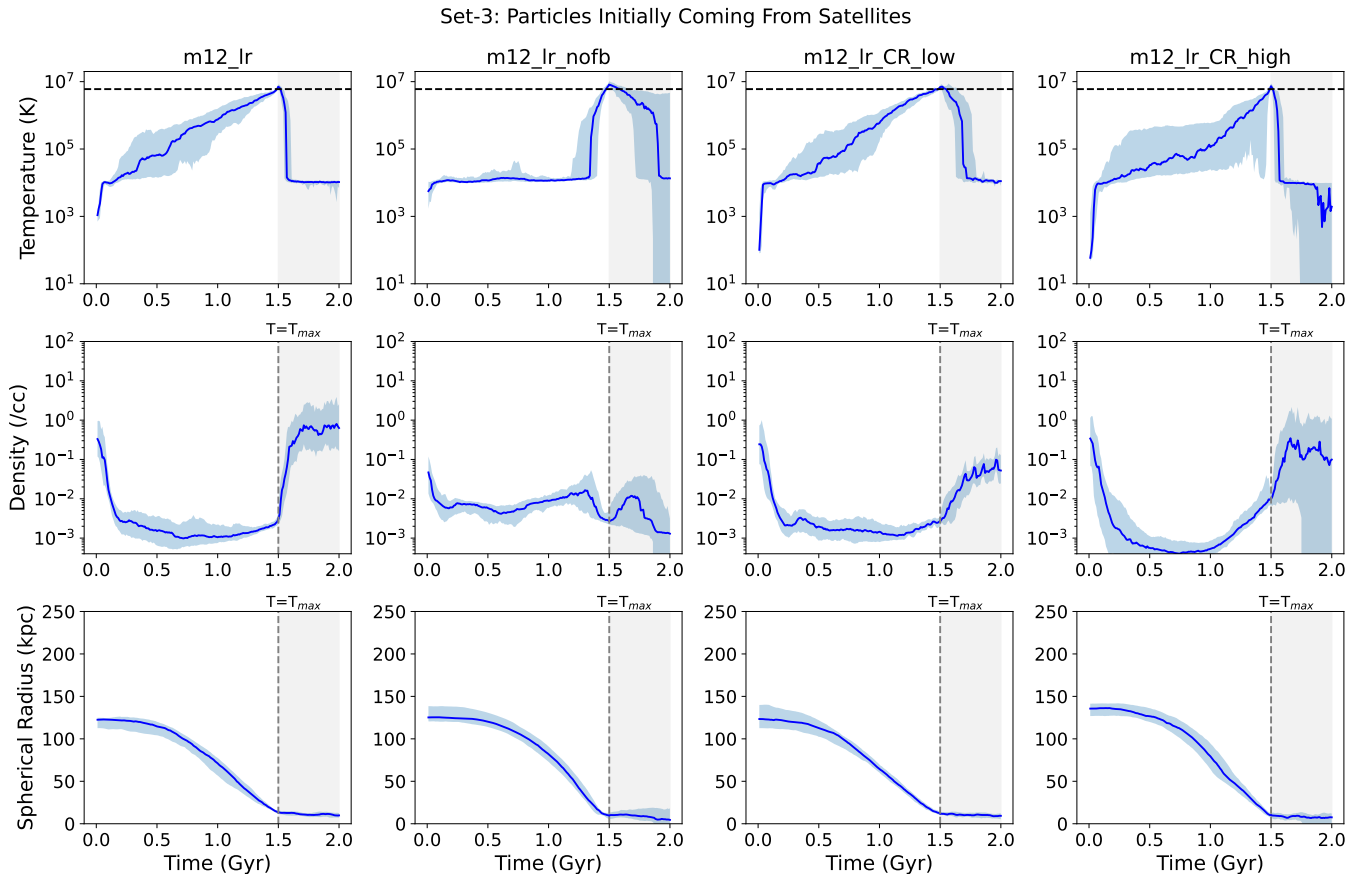


Figure 6. Time evolution of the temperature (top row), density (2nd row), and spherical radius (bottom row) of gas particles initially coming from satellites, which reached their maximum temperature at a simulation time of 1.5 Gyr. The solid lines represent the median values of the gas properties, while the shaded regions indicate the dispersion. The figure illustrates how infalling gas originating from satellites is heated to super-virial temperatures through compressive heating.

lar feedback, hence are absent in no feedback case and are more in high CR case due to the additional heating from CR feedback by larger amount of CR.

In the middle row of Figure 4, we plot past density of these gas particles. All of them start from 10^{-2}cm^{-3} and finally become 10^2cm^{-3} right before the heating up at 1 Gyr. Then their density again drops down to 10^{-2}cm^{-3} once they heated up by feedback. In bottom row of Figure 4, we plot the past position of these super-virial gas. All of them remain in the 10 kpc to 20 kpc region.

Thus, we see that these set-2 gas particles represent the cold ISM gas, which gets colder and denser over time and may form stars. Then they suddenly heat up by stellar feedback. However, set-2 gas particles are less than 0.01 times the set-1 gas particles. As we can see in Figure 5, the fraction of total supervirial gas host mass is $\sim 1\%$ due to feedback and $\sim 99\%$ due to compressive heating. This implies the mass in the supervirial phase as traced by set-2 gas particles is smaller by a factor of

~ 100 , hence set-2 gas particles contribute very little to super-virial gas mass budget.

3.4.3. Set-3: Particles Initially Coming From Satellites

There is another set of gas particles that can heat up to super-virial temperature, as shown in Figure 6. The gas from satellites gets stripped and falls inward. As they accrete onto the galactic disc, they heat up due to the gravitational potential energy loss and compression, just as the set-1 gas particles. We showed in the Figure 5, that the fraction in this set is initially zero but starts developing at the time-scale of satellite gas infall, around 1.2 Gyr. It starts with as low as 0.1% of the supervirial budget, but slowly goes up to even 10% at 1.5 Gyr. Therefore, at later time, the contribution from satellite gas phase can also contribute to supervirial gas phase significantly.

3.5. What distinguishes gas which heats up to super-virial temperatures?

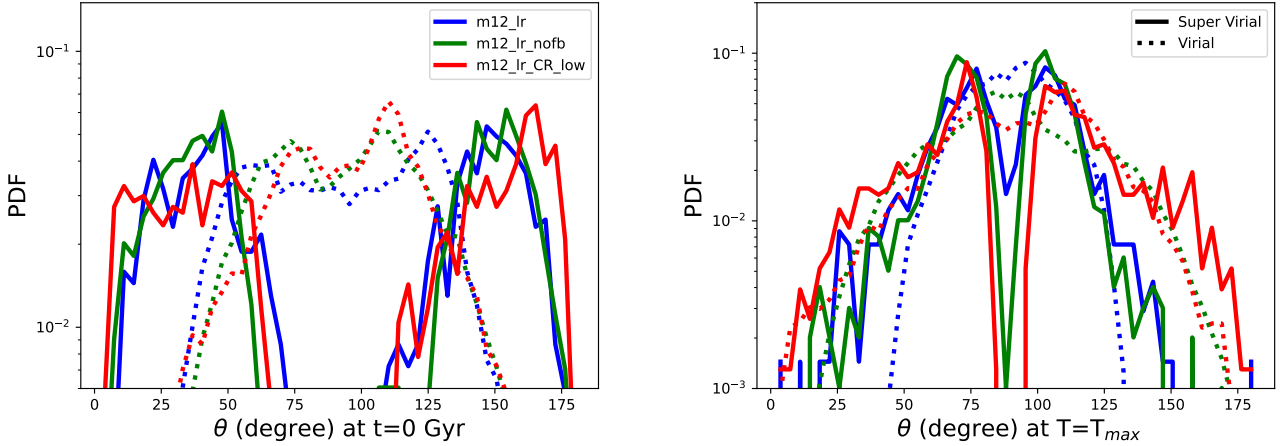


Figure 7. Probability distribution function of the angle to the galaxy rotation axis at $t = 0$ Gyr (left panel) and at maximum temperature T_{\max} (right panel), for all infalling gas particles with a virial temperature beyond 20 kpc. Dotted and solid lines indicate virial and super-virial temperatures within 20 kpc at $t=1$ Gyr, respectively. Gas which heats up to super-virial temperatures starts closer to the rotation axis, while gas farther from the axis remains at virial temperatures. The right panel shows that when the gas reaches super-virial temperatures it is more uniformly distributed across the disk than initially.

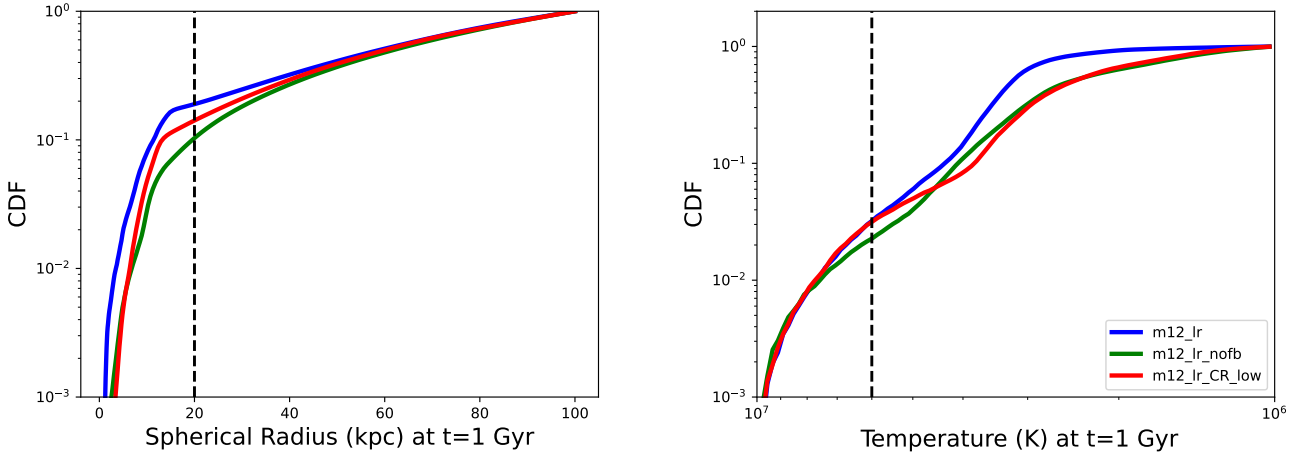


Figure 8. Cumulative distribution function (CDF) of the spherical radius (left panel) and temperature (right panel) at $t=1$ Gyr of gas particles that start at virial temperature beyond 20 kpc at $t=0$ Gyr. The figure demonstrates that around 10-15% of the gas is found within 20 kpc at $t = 1$ Gyr. About 1% of this infalling virial gas is heated up to super-virial temperatures.

Orange curves in Figure 3 plot the time evolution of the temperature (top row), density (2nd row), spherical radius (3rd row), and scale height (bottom row) of infalling virial gas particles that do not get heated up to super-virial temperatures. As we can see, they are also falling inwards, and as they do that, the temperature and density of the gas increases.

In Figure 7, we investigate the distribution of probability distribution function of the angle (θ) to the galaxy rotation axis at $t = 0$ Gyr (left panel) and at maximum temperature (right panel), for all infalling gas particles with a virial temperature beyond 20 kpc. In the

Left panel, we can see the gas particles that heat up to super-virial temperatures are closer to the rotation axis, whereas the gas particles that remain at virial temperature are further from the rotation axis. It implies that infalling virial gas which originates from close to the rotation axis reaches higher temperatures. This is consistent with the behavior of rotating hot inflows (or ‘rotating cooling flows’) where the hot CGM phase inflows and spins up on a cooling timescale (Hafen et al. 2022; Stern et al. 2024). In these accretion flows gas has lower densities near the rotation axis, due to rotation support (see figure 4f in Stern et al. 2024). When the hot

inflow approaches the disk, it transitions from a spherical geometry to a disk geometry. During this change in geometry, gas particles near the rotation axis suffer smaller radiative losses (which scale as density squared, see figure 4k there), and experience larger compressive heating rates (which scale inversely with density, see figure 4l there).

Supporting the rotating hot inflow interpretation, the right panel of Figure 7 shows that the θ distribution when the temperature is maximal is close to 90 degrees, distinctly different from the initial θ distribution. This means that the super-virial gas particles have indeed transitioned from a spherical to a disk geometry. Further support for this interpretation is that the gas cools immediately after reaching super-virial temperatures (Figure 3), as expected in rotating hot inflows which cool immediately onto the ISM after transition into a disk geometry (Stern et al. 2024).

Therefore, some of the virial temperature gas is infalling from outer CGM (50 – 60 kpc) to the inner CGM (20 – 10 kpc). All of this inflowing gas loses gravitational energy and is heated up by a factor of 1.5 – 2. When it reaches the inner CGM, the gas gets further heated up by another factor of 1.5 – 2 due to compressive heating when the hot inflow changes from a spherical to a disc geometry. This change in geometry is instigated by rotation support in the hot inflow. Immediately thereafter, the hot inflow cools and joins the ISM disc. Specifically, inflowing virial gas closer to the rotation axis of the galaxy suffers less radiative cooling and more compressive heating due to lower gas density near the axis, and therefore heats up more.

3.6. *What amount of infalling virial gas heats up to super-virial phase?*

To investigate how much virial gas is infalling, we calculate a cumulative distribution function (CDF) of the final position (at $t = 1$ Gyr) of the gas particles which starts at virial temperature beyond 20 kpc at $t = 0$ Gyr. In the left panel of Figure 8, we show that only 10% gas particles enter 20 kpc at $t = 1$ Gyr. With these gas particles which are 20 kpc at $t = 1$ Gyr, we make a CDF of temperature distribution in right panel of Figure 8, where we see only 1-2% of these gas will heat up to super-virial temperatures.

3.7. *Fate of this super-virial gas*

This supervirial gas will also eventually cools down once it is supported by rotation, as we see in Figure 3, 4, and 6. In these figures, we denote the grey-shaded region to be the time evolution of the gas after they become super virial. We can see all the supervirial gas

cools down in the later snapshot, consistent with the hot rotating inflow solution discussed in Stern et al. (2024). But the cooled gas will immediately be replenished by heating of continuously inflowing virial gas by the same process. Therefore, we see a constant amount of super-virial gas over time.

To summarize, we investigate mechanisms driving the heating of virial gas within a galaxy, finding that gas particles exhibit distinct heating behaviors based on their initial conditions and interactions. Set-1 gas particles, originating from the halo, closer to the rotation axis, heat up as they infall where the gas converts gravitational energy to heat mainly via compressive heating. This process causes gas infalling close to the rotation axis to reach super-virial temperatures just before cooling and joining the disk. In contrast, set-2 gas particles, likely representing the cold ISM gas, heat up sporadically, potentially due to stellar feedback, contribute minimally to the super-virial gas mass budget. Additionally, gas particles stripped from satellites and accreting onto the disc also heat up via compressive heating, further contributing to the super-virial phase. Some virial gas particles fail to heat up to supervirial temperature as they infall further from the rotation axis hence suffers more radiative cooling and less compressive heating.

4. DISCUSSION, LIMITATIONS AND FUTURE WORK

We also investigate the temperature profile in a run where the virial temperature phase of the CGM is initialized with a cooling flow rather than hydrostatic equilibrium, using the cooling flow solution from Stern et al. (2019). We find that our cooling flow run also produces super-virial gas within 20 kpc and its mass is of the same order as the other runs (Figure 2). This makes sense since HSE initial conditions are expected to develop into a cooling flow within a cooling time (Stern et al. 2019).

Bottom panel of Figure 3 and right panel of Figure 7 clearly indicates that the super-virial gas is extra-planar, just above the ISM disk. It will thus be very interesting to investigate future X-ray observations of edge-on galaxies, which we will discuss in the follow-up paper. In future work, we will also post process and produce observable like X-ray emission and absorption maps from the simulation snapshots. This will both facilitate direct comparison with observed maps, and assist in distinguishing between emission and absorption origins.

It is fascinating to see that conventional CR/feedback heating do not produce this super-virial phase as anticipated, whereas gravitational and compressive heating is the dominant heating mechanisms in our idealized

GIZMO simulations with FIRE stellar feedback model. However, this still depends on the feedback prescription used in the simulation. With a different feedback prescription (e.g., [Smith et al. 2024b,a](#)), one may get a different result. For example, the idealized simulation by the recent work of [Vijayan & Li \(2022\)](#) reproduced this temperature component, likely to be caused due to heating by stellar feedback, but with a very high star-formation rate unlike the MW. Another recent work by [Singh Bisht et al. \(2024\)](#) conclude that the super-virial gas is a result of the stellar feedback in their idealized simulation. Additionally, we do not have AGN feedback, that can have larger impact than stellar feedback in terms of heating the gas (e.g., [Weinberger et al. 2023](#); [Cochrane et al. 2023](#); [Qutob et al. 2023](#); [Su et al. 2024](#)). For example, a recent work by [Ramesh et al. \(2023\)](#) also examines the physical properties of gas within the CGM surrounding 132 MW-like central galaxies at a redshift of $z=0$, using data from the cosmological simulation TNG50, which is part of the IllustrisTNG project. They found that energy from supermassive black hole (SMBH)-driven kinetic winds heats up the gas to super-virial temperatures (exceeding $10^{6.5}$ to 10^7 K). Therefore, it would be useful to explore several different simulations and investigate the similar questions to compare. It will not only give us an overall picture of this newly-found super-virial phase, but also can constrain varying feedback mechanisms in different simulations.

Also, another limitations of our work is that it does not consider the galaxy in cosmological context. Our future works will explore the same questions with different cosmological simulations such as FIRE zoom-in runs ([Hopkins et al. 2018b, 2023](#); [Wellons et al. 2023](#)), HESITA ([Libeskind et al. 2020](#)), TNG ([Weinberger et al. 2017](#); [Pillepich et al. 2018](#)) and EAGLE ([Crain et al. 2015](#); [Schaye et al. 2015](#)) simulations. These insights will deepen our understanding of galactic gas dynamics and provide valuable implications for broader inquiries into galaxy evolution and structure formation.

5. CONCLUSIONS

Several observations have recently established that the MW contains gas at temperatures higher than its virial temperature. However, location, origin and properties of this gas are still unknown. In this paper, we analyze a suite of idealized simulations to investigate this newly-discovered gas phase and find this super-virial phase gas in our simulations of a MW-like galaxy. Our main findings are the following:

- Most of the super-virial gas is within 20 kpc from the center of the galaxy (Left Panel of Figure 1),

which implies they are situated mostly in extended disc region, not in the CGM.

- This super-virial gas phase is found close to the disk where typical gas densities are $\leq 10^{-2}\text{cm}^{-3}$ (Right Panel of Figure 1 and 3rd panel of Figure 3, and bottom panel 4).
- The mass of this gas is roughly constant, in the range $1 - 2 \times 10^7 M_{\odot}$. This phase is retained in the simulations even at 1.5 Gyr (Figure 2).
- We also investigate the effect of stellar feedback in heating up the gas. We see no change in the gas mass in the case of no feedback run (Figure 2). However, we see that some cold 10^4 K gas in the central galaxy is heated up to super-virial phase which is absent in no feedback run. However, the feedback heating contributes only less than 1% of the super-virial gas, implying this mechanism of heating is sub-dominant, at least for the FIRE-feedback prescription (Figure 5).
- We also explore effect of CR in the heating of the gas. With high and low CR initial setup, we found no change in the super virial gas mass hence implying that the CR has little role in heating up the gas to super-virial temperatures (Figure 2).
- While investigating the origin of super-virial gas, we found that the dominant contribution to heating is caused by a rotating inflow of the virial CGM phase as in the model of [Stern et al. \(2024\)](#). In this model gravitational energy is converted to heat mainly via compressive heating in the inflow. We show this process causes the 1-2% of gas infalling closest to the rotation axis to reach super-virial temperatures just before cooling and joining the disk (Figs. 7, 8). Gas inflowing near the rotation axis has a lower density and thus suffers less cooling losses and is more compressively heated than gas farther away from the axis, allowing it to reach higher temperatures. Gas stripped from satellites also inflows onto central galaxy and heats up similarly (Figure 6).

In conclusion, we identify compressive heating of the hot inflow as a significant contributor to the super-virial gas in the Milky Way. However, several caveats require further investigation in future studies, including more detailed comparisons with observational data (see Section 4).

ACKNOWLEDGMENTS

We also thank FIRE collaboration for useful discussions and suggestions. MR acknowledges support from the Center for Cosmology and particle physics fellowship at Ohio State University. MR acknowledges ACCESS allocations PHY240003. MR also acknowledges Aspen Center for Physics and Simons Foundation as this work was performed in part at the Aspen Center for Physics, which is supported by a grant from the Simons Foundation (1161654, Troyer). KS acknowledges support from

the Black Hole Initiative at Harvard University, which is funded by grants from the John Templeton Foundation and the Gordon and Betty Moore Foundation, and acknowledges ACCESS allocations TG-PHY220027 and TG-PHY220047 and Frontera allocation AST22010. JS was supported by the Israel Science Foundation (grant No. 2584/21). The computations in this work were run at facilities supported by the Bridges, University of Pittsburgh.

REFERENCES

- Bhattacharyya, J., Das, S., Gupta, A., Mathur, S., & Krongold, Y. 2023, *ApJ*, 952, 41, doi: [10.3847/1538-4357/acd337](https://doi.org/10.3847/1538-4357/acd337)
- Bluem, J., Kaaret, P., Kuntz, K. D., et al. 2022, *VizieR Online Data Catalog: HaloSat survey of the Galactic CGM (Bluem+, 2022)*, *VizieR On-line Data Catalog: J/ApJ/936/72*. Originally published in: 2022ApJ...936...72B, doi: [10.26093/cds/vizieer.19360072](https://doi.org/10.26093/cds/vizieer.19360072)
- Chan, T. K., Kereš, D., Hopkins, P. F., et al. 2019a, *MNRAS*, 488, 3716, doi: [10.1093/mnras/stz1895](https://doi.org/10.1093/mnras/stz1895)
- . 2019b, *MNRAS*, 488, 3716, doi: [10.1093/mnras/stz1895](https://doi.org/10.1093/mnras/stz1895)
- Cochrane, R. K., Anglés-Alcázar, D., Mercedes-Feliz, J., et al. 2023, *MNRAS*, 523, 2409, doi: [10.1093/mnras/stad1528](https://doi.org/10.1093/mnras/stad1528)
- Crain, R. A., Schaye, J., Bower, R. G., et al. 2015, *MNRAS*, 450, 1937, doi: [10.1093/mnras/stv725](https://doi.org/10.1093/mnras/stv725)
- Das, S., Mathur, S., Gupta, A., & Krongold, Y. 2021, *ApJ*, 918, 83, doi: [10.3847/1538-4357/ac0e8e](https://doi.org/10.3847/1538-4357/ac0e8e)
- Das, S., Mathur, S., Gupta, A., Nicastro, F., & Krongold, Y. 2019a, *ApJ*, 887, 257, doi: [10.3847/1538-4357/ab5846](https://doi.org/10.3847/1538-4357/ab5846)
- Das, S., Mathur, S., Nicastro, F., & Krongold, Y. 2019b, *ApJL*, 882, L23, doi: [10.3847/2041-8213/ab3b09](https://doi.org/10.3847/2041-8213/ab3b09)
- Fang, T., Buote, D., Bullock, J., & Ma, R. 2015, *ApJS*, 217, 21, doi: [10.1088/0067-0049/217/2/21](https://doi.org/10.1088/0067-0049/217/2/21)
- Faucher-Giguère, C.-A., & Oh, S. P. 2023, *ARA&A*, 61, 131, doi: [10.1146/annurev-astro-052920-125203](https://doi.org/10.1146/annurev-astro-052920-125203)
- Guo, F., & Oh, S. P. 2008, *MNRAS*, 384, 251, doi: [10.1111/j.1365-2966.2007.12692.x](https://doi.org/10.1111/j.1365-2966.2007.12692.x)
- Gupta, A., Mathur, S., Kingsbury, J., Das, S., & Krongold, Y. 2023, *Nature Astronomy*, 7, 799, doi: [10.1038/s41550-023-01963-5](https://doi.org/10.1038/s41550-023-01963-5)
- Gupta, A., Mathur, S., Krongold, Y., Nicastro, F., & Galeazzi, M. 2012, *ApJL*, 756, L8, doi: [10.1088/2041-8205/756/1/L8](https://doi.org/10.1088/2041-8205/756/1/L8)
- Hafen, Z., Stern, J., Bullock, J., et al. 2022, *MNRAS*, 514, 5056, doi: [10.1093/mnras/stac1603](https://doi.org/10.1093/mnras/stac1603)
- Henley, D. B., & Shelton, R. L. 2013, *ApJ*, 773, 92, doi: [10.1088/0004-637X/773/2/92](https://doi.org/10.1088/0004-637X/773/2/92)
- Hopkins, P. F. 2015, *MNRAS*, 450, 53, doi: [10.1093/mnras/stv195](https://doi.org/10.1093/mnras/stv195)
- . 2016, *MNRAS*, 462, 576, doi: [10.1093/mnras/stw1578](https://doi.org/10.1093/mnras/stw1578)
- . 2017, *MNRAS*, 466, 3387, doi: [10.1093/mnras/stw3306](https://doi.org/10.1093/mnras/stw3306)
- Hopkins, P. F., & Raives, M. J. 2016, *MNRAS*, 455, 51, doi: [10.1093/mnras/stv2180](https://doi.org/10.1093/mnras/stv2180)
- Hopkins, P. F., Wetzel, A., Kereš, D., et al. 2018a, *MNRAS*, 477, 1578, doi: [10.1093/mnras/sty674](https://doi.org/10.1093/mnras/sty674)
- . 2018b, *MNRAS*, 480, 800, doi: [10.1093/mnras/sty1690](https://doi.org/10.1093/mnras/sty1690)
- Hopkins, P. F., Wetzel, A., Wheeler, C., et al. 2023, *MNRAS*, 519, 3154, doi: [10.1093/mnras/stac3489](https://doi.org/10.1093/mnras/stac3489)
- Kroupa, P. 2002, *Science*, 295, 82, doi: [10.1126/science.1067524](https://doi.org/10.1126/science.1067524)
- Lara-DI, A., Mathur, S., Krongold, Y., Das, S., & Gupta, A. 2023, *ApJ*, 946, 55, doi: [10.3847/1538-4357/acbf40](https://doi.org/10.3847/1538-4357/acbf40)
- Leitherer, C., Schaerer, D., Goldader, J. D., et al. 1999, *ApJS*, 123, 3, doi: [10.1086/313233](https://doi.org/10.1086/313233)
- Libeskind, N. I., Carlesi, E., Grand, R. J. J., et al. 2020, *MNRAS*, 498, 2968, doi: [10.1093/mnras/staa2541](https://doi.org/10.1093/mnras/staa2541)
- Mathur, S. 2022 (Springer Nature Singapore), doi: [10.1007/978-981-16-4544-0_112-1](https://doi.org/10.1007/978-981-16-4544-0_112-1)
- McClain, R. L., Mathur, S., Das, S., Krongold, Y., & Gupta, A. 2024, *MNRAS*, 527, 5093, doi: [10.1093/mnras/stad3497](https://doi.org/10.1093/mnras/stad3497)
- Nakashima, S., Inoue, Y., Yamasaki, N., et al. 2018, *ApJ*, 862, 34, doi: [10.3847/1538-4357/aacceb](https://doi.org/10.3847/1538-4357/aacceb)
- Pfrommer, C., Pakmor, R., Schaal, K., Simpson, C. M., & Springel, V. 2017a, *MNRAS*, 465, 4500, doi: [10.1093/mnras/stw2941](https://doi.org/10.1093/mnras/stw2941)
- Pfrommer, C., Pakmor, R., Simpson, C. M., & Springel, V. 2017b, *ApJL*, 847, L13, doi: [10.3847/2041-8213/aa8bb1](https://doi.org/10.3847/2041-8213/aa8bb1)
- Pillepich, A., Springel, V., Nelson, D., et al. 2018, *MNRAS*, 473, 4077, doi: [10.1093/mnras/stx2656](https://doi.org/10.1093/mnras/stx2656)
- Ponti, G., Zheng, X., Locatelli, N., et al. 2023, *A&A*, 674, A195, doi: [10.1051/0004-6361/202243992](https://doi.org/10.1051/0004-6361/202243992)

- Qutob, N., Emami, R., Su, K.-Y., et al. 2023, arXiv e-prints, arXiv:2312.14809, doi: [10.48550/arXiv.2312.14809](https://doi.org/10.48550/arXiv.2312.14809)
- Ramesh, R., Nelson, D., & Pillepich, A. 2023, MNRAS, 518, 5754, doi: [10.1093/mnras/stac3524](https://doi.org/10.1093/mnras/stac3524)
- Roy, M., Su, K.-Y., Tonnesen, S., Fielding, D. B., & Faucher-Giguère, C.-A. 2024, MNRAS, 527, 265, doi: [10.1093/mnras/stad3142](https://doi.org/10.1093/mnras/stad3142)
- Schaye, J., Crain, R. A., Bower, R. G., et al. 2015, MNRAS, 446, 521, doi: [10.1093/mnras/stu2058](https://doi.org/10.1093/mnras/stu2058)
- Shen, S., Madau, P., Guedes, J., et al. 2013, ApJ, 765, 89, doi: [10.1088/0004-637X/765/2/89](https://doi.org/10.1088/0004-637X/765/2/89)
- Singh Bisht, M., Nath, B. B., & Mathur, S. 2024, arXiv e-prints, arXiv:2408.14344, doi: [10.48550/arXiv.2408.14344](https://doi.org/10.48550/arXiv.2408.14344)
- Smith, M. C., Fielding, D. B., Bryan, G. L., et al. 2024a, arXiv e-prints, arXiv:2408.15321, doi: [10.48550/arXiv.2408.15321](https://doi.org/10.48550/arXiv.2408.15321)
- . 2024b, MNRAS, 527, 1216, doi: [10.1093/mnras/stad3168](https://doi.org/10.1093/mnras/stad3168)
- Snowden, S. L., Freyberg, M. J., Kuntz, K. D., & Sanders, W. T. 2000, ApJS, 128, 171, doi: [10.1086/313378](https://doi.org/10.1086/313378)
- Springel, V. 2000, MNRAS, 312, 859, doi: [10.1046/j.1365-8711.2000.03187.x](https://doi.org/10.1046/j.1365-8711.2000.03187.x)
- Springel, V., & White, S. D. M. 1999, MNRAS, 307, 162, doi: [10.1046/j.1365-8711.1999.02613.x](https://doi.org/10.1046/j.1365-8711.1999.02613.x)
- Stern, J., Fielding, D., Faucher-Giguère, C.-A., & Quataert, E. 2019, MNRAS, 488, 2549, doi: [10.1093/mnras/stz1859](https://doi.org/10.1093/mnras/stz1859)
- Stern, J., Fielding, D., Hafen, Z., et al. 2024, MNRAS, 530, 1711, doi: [10.1093/mnras/stae824](https://doi.org/10.1093/mnras/stae824)
- Su, K.-Y., Hopkins, P. F., Hayward, C. C., et al. 2017, MNRAS, 471, 144, doi: [10.1093/mnras/stx1463](https://doi.org/10.1093/mnras/stx1463)
- . 2019a, MNRAS, 487, 4393, doi: [10.1093/mnras/stz1494](https://doi.org/10.1093/mnras/stz1494)
- . 2019b, MNRAS, 487, 4393, doi: [10.1093/mnras/stz1494](https://doi.org/10.1093/mnras/stz1494)
- Su, K.-Y., Bryan, G. L., Hayward, C. C., et al. 2024, MNRAS, 532, 2724, doi: [10.1093/mnras/stae1629](https://doi.org/10.1093/mnras/stae1629)
- Tumlinson, J., Peebles, M. S., & Werk, J. K. 2017, ARA&A, 55, 389432, doi: [10.1146/annurev-astro-091916-055240](https://doi.org/10.1146/annurev-astro-091916-055240)
- Tumlinson, J., Thom, C., Werk, J. K., et al. 2011, Science, 334, 948, doi: [10.1126/science.1209840](https://doi.org/10.1126/science.1209840)
- Uhlig, M., Pfrommer, C., Sharma, M., et al. 2012, MNRAS, 423, 2374, doi: [10.1111/j.1365-2966.2012.21045.x](https://doi.org/10.1111/j.1365-2966.2012.21045.x)
- Vijayan, A., & Li, M. 2022, MNRAS, 510, 568, doi: [10.1093/mnras/stab3413](https://doi.org/10.1093/mnras/stab3413)
- Weinberger, R., Springel, V., Hernquist, L., et al. 2017, MNRAS, 465, 3291, doi: [10.1093/mnras/stw2944](https://doi.org/10.1093/mnras/stw2944)
- Weinberger, R., Su, K.-Y., Ehlert, K., et al. 2023, MNRAS, 523, 1104, doi: [10.1093/mnras/stad1396](https://doi.org/10.1093/mnras/stad1396)
- Wellons, S., Faucher-Giguère, C.-A., Hopkins, P. F., et al. 2023, MNRAS, 520, 5394, doi: [10.1093/mnras/stad511](https://doi.org/10.1093/mnras/stad511)
- Werk, J. K., Prochaska, J. X., Cantalupo, S., et al. 2016, ApJ, 833, 54, doi: [10.3847/1538-4357/833/1/54](https://doi.org/10.3847/1538-4357/833/1/54)